MDPI

Article

Distinct fracture patterns in construction steels for reinforced concrete – a review.

Fernando Suárez [1,†], Jaime C. Gálvez [2], David A. Cendón [3] and J. M. Atienza [3*]

[1] Departamento de Ingeniería Mecánica y Minera. Universidad de Jaén; fsuarez@ujaen.es
[2] Departamento de Ingeniería Civil- Construcción. Universidad Politécnica de Madrid . E.T.S.I. Caminos, Canales y Puertos; jaime.galvez@upm.es
[3] Departamento de Ciencia de Materiales, Universidad Politécnica de Madrid . E.T.S.I. Caminos, Canales y Puertos; david.cendon.franco@upm.es and josemiguel.atienza@upm.es
* Correspondence: fsuarez@ujaen.es; Tel.: +034-953-648-606
† Current address: Departamento de Ingeniería Mecánica y Minera. Universidad de Jaén. Campus Científico-Tecnológico de Linares. Cinturón Sur 23700-Linares (Jaén)

Academic Editor: name
Version February 20, 2018 submitted to Metals

Abstract: Steel is one of the most widely used materials in construction. Nucleation growth and coalescence theory is usually employed to explain the fracture process in ductile materials, such as many metals. The typical cup-cone fracture pattern has been extensively studied in the past, giving rise to numerical models able to reproduce this pattern. Nevertheless, some steels, such as the eutectoid steel used for manufacturing prestressing wires, does not show this specific shape but a flat surface with a dark region in the centre of the fracture area. Late studies have deepened the knowledge on these distinct fracture patterns, giving light on some aspects that help to understand how damage begins and propagates in each case. The numerical modelling of both fracture patterns have also been discussed and reproduced with different approaches. This work reviews the main lately advances in the knowledge on this subject, particularly focusing on the experimental work carried out by the authors.

Keywords: Steel; Fracture Mechanics; Tensile Test; Cohesive zone model; Internal damage; XRCT.

1. Introduction

Steel is, with concrete, the most extended material in construction and civil engineering works. Its strength and ductility make it of special interest when addressing structural safety issues, since it enables stress distribution with adjacent elements, allowing a higher ammount of energy to dissipate before failure. However, some aspects related with its failure behaviour remain unclear, especially in those steels that do not present the classical cup-cone fracture surface, which has been extensely studied in the past.

The mechanical characterization of this type of materials is usually reduced to obtaining their elastic parameters, elastic modulus E and Poisson's ratio ν. These values are generally obtained by means of a tensile test, which is standardised by EN ISO 6892 [1], and allows obtaining with precision the load-strain diagram up to the maximum loading point. Nevertheless, difficulties arise when the behaviour after the maximum load point needs to be defined, which usually leads to neglecting that information of the test. This final part of the load-strain diagram is, however, of great interest since it is directly related to the maximum energy that can be absorbed by an structural element before collapsing, which goes together with the structural safety and may help, for instance, to distinguish between accidental damage and induced damage.

Regarding the construction steels fracture mechanisms, the cup-cone fracture pattern, typical of very ductile steels and shown in Figure 1b), is very well known and has been extensively studied in the past [3–10]. The mechanisms involved in it are clearly identified: the central zone corresponds to a process of nucleation, growth and coalescence of microvoids while the surrounding inclined lips, usually referred to as shear lips [3,11], develop due to cleavage. Nevertheless, not all steels show the same fracture behaviour, for instance, the pearlitic steel used for manufacturing prestressing wires presents a flat fracture surface, perpendicular to the loading direction and with a circular dark area in the center (see Figure 1a)). For the sake of clarity, in the rest of the text the flat pattern will be referred to as type 1 and the cup-cone pattern as type 2.

Other authors have studied the steel used in prestressing steel wires, which shows the flat fracture pattern called type 1, focusing their interest on the effect of cold-drawing on the developed fracture mechanism [12–14].

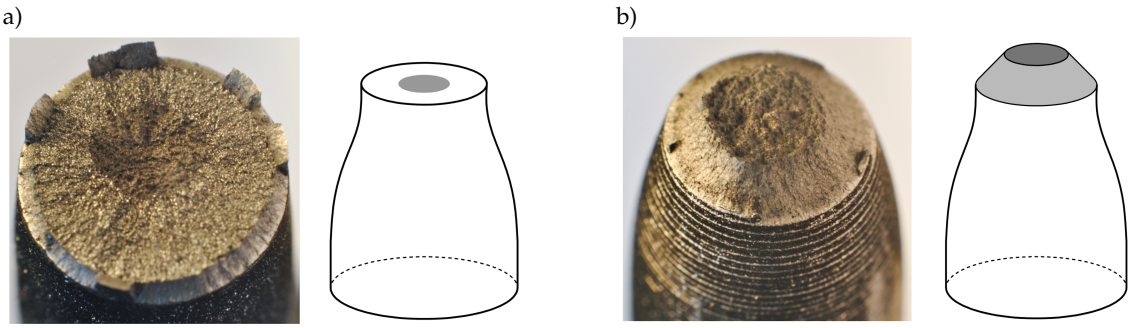

Figure 1. Fracture surfaces on 9mm-diameter specimens of two steels with different fracture patterns after testing under tension: a) Fracture pattern type 1, b) Fracture pattern type 2 [15].

Despite the characteristics of steels have been studied for a long time, there are still some issues that remain unclear, especially regarding the plastic behaviour after maximum loading and, more precisely, the mechanisms that unchain final failure in steels exhibiting different fracture patterns. The objective of this work is to review recent experimental and numerical advances dealing with fracture mechanics in steels, with special emphasis on the type 1 pattern, flat fracture surface, since the type 2, cup-cone pattern, is better known and has been widely studied in the past. Firstly, some relevant experimental results that analyse both fracture patterns are presented and secondly, the main numerical models used with metals are briefly overviewed, also describing a lately approach based on Linear Elastic Fracture Mechanics (LEFM) considerations.

2. Experimental results on steel specimens under tensile loading

The following results correspond to two steels that are representative of both mentioned fracture patterns. Table 1 shows their chemical composition, with Material 1 being an eutectoid steel used for manufacturing prestressing wires before cold-drawing, which exhibits fracture pattern type 1 and Material 2 a low-carbon steel ($< 0.24\%$C), used as reinforcement in concrete structures, which shows the fracture pattern denoted as type 2.

Table 1. Chemical composition of both materials in %.

Mat.	C	Si	Mn	P	S	Cr	Mo	Ni	Cu	Al	Ti	Nb	V	N
1	0.83	0.25	0.72	0.012	0.004	0.24	<0.01	0.02	0.01	<0.003	<0.005	<0.005	<0.01	0.0097
2	0.22	0.18	1.00	0.024	0.042	0.08	0.03	0.14	0.46	<0.003	<0.005	<0.005	<0.01	0.0113

2.1. Stress-strain diagrams

When a steel bar is tested under tension there are several issues that may affect the results, such as the specimen length, the specimen radius, the initial gage length used or even the technique employed for measuring strain. For a complete description of the following results, the reader is referred to [15,16].

2.1.1. Strain measuring technique

As already mentioned, the last part of the stress-strain diagram is usually discarded because when the specimen is loaded beyond its maximum bearing capacity, strain is localised in a necking region which makes the analysis difficult. In fact, this is true if the classical strain measuring devices are used, such as conventional extensometers as that shown in Figure 2a), which only provide information of elongation between two especific points in the specimen and their results are only valid up to the maximum load point, since necking may take place out of the gauge length or, at least, not centered with the reference points used to measure strain. Nevertheless, in the last decades digital image correlation systems (DIC) have become widely extended, which overcome this limitation [17–22]. These systems use one or two high-definition video cameras (depending on whether results are needed in 2D or 3D), which record a marked specimen throughout the test; Figure 2b) shows the experimental setup for a 2D case. The obtained pictures are postprocessed with a especific software that can keep track of the speckles marked on the specimen surface, providing relative displacements between any desired pair of points or even providing a strain mapping of the specimen surface. This has a major advantage for analysing the last part of the stress-strain diagram in a tensile test: the deformation can always be tracked between points that are equally spaced from the eventual fracture plane.

a) b)

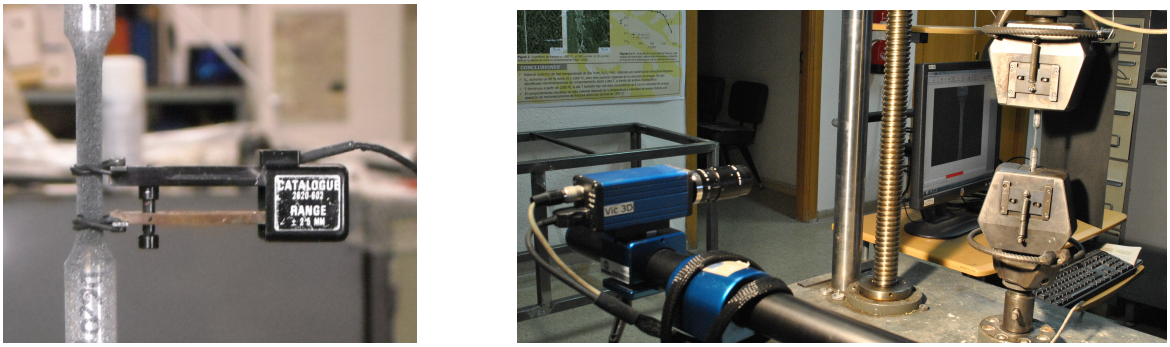

Figure 2. a) A conventional extensometer on a cylindrical specimen, b) Setup for measuring strains with a digital image correlation system [16]

Figure 3 shows the fracture diagram obtained for a tensile test where strain was monitored with both systems; DIC proves its capability for providing data up to the eventual fracture instant, while the conventional extensometer only provides valid information up to the maximum load point. Therefore, if DIC systems are used for monitoring strain, there is in principle no reason why the information obtained after peak should be neglected.

2.1.2. Influence of the specimen radius and the initial gauge length

When testing a cylindrical steel bar under tension, several parameters must be defined, such as the initial gauge length and the diameter and length of the specimen. Figures 4 and 5 show several engineering stress-strain diagrams for Materials 1 and 2, respectively; all tests were monitored with DIC, so the strain was measured with a gauge length centered with the fracture cross-section and obtained up to the eventual failure of the specimen. Three specimen diameters were considered, 3 mm,

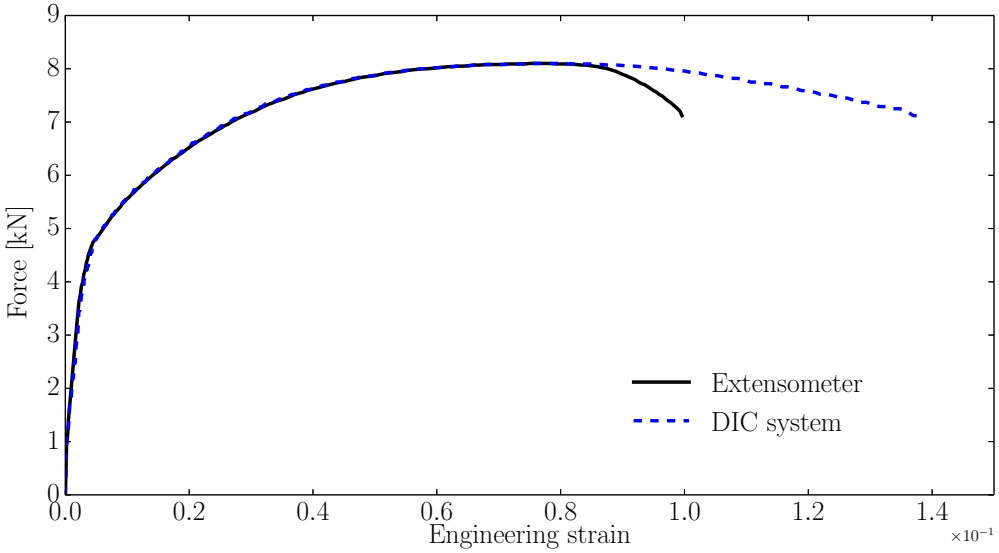

Figure 3. Force-engineering strain curves of a tensile test simultaneaously obtained with a conventional extensometer and a DIC system [16]

6 mm and 9 mm, and three gauge lengths compared, one of them of a fixed length equal to 12.5 mm and two proportional to the specimen diameter, once and twice the specimen diameter.

In both materials, when proportional-to-the-diameter gauge lenths are considered, the results obtained are always similar, no matter the specimen diameter, but when a fixed gauge length is employed, clear differences are found. When necking develops, the strain field is not uniform anymore along the specimen and concentrates on very localised region of the bar; therefore, strains measured with a fixed gauge length on specimens of different diameters provide a certain average strain that cannot be compared among them. See section 2.2 for further details.

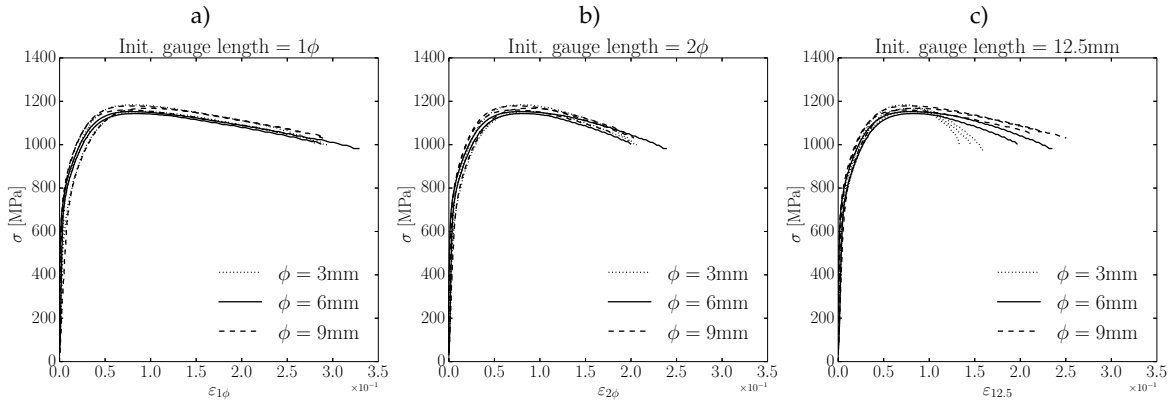

Figure 4. $\sigma - \varepsilon$ curves obtained with Material 1 specimens of distinct radii and using several initial gauge lengths: a) initial gauge length=1ϕ, a) initial gauge length=2ϕ, a) initial gauge length=12.5 mm. [23]

2.1.3. Influence of the specimen length

The length of the constant cross-section length in a specimen (L_1 in Figure 6a)) is limited by the standards to avoid too short specimens that cannot develop the whole necking process. In principle, once the specimen dimensions meet the requirements defined in [1], this can be designed with any

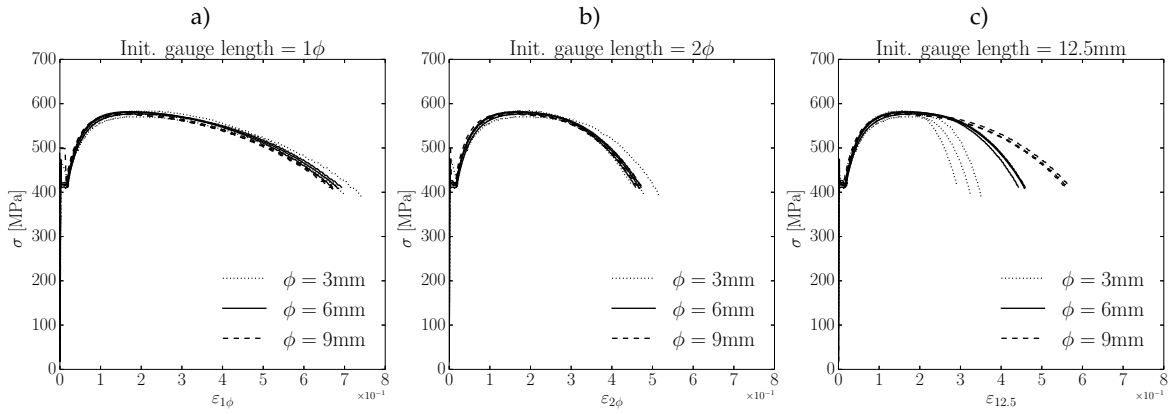

Figure 5. $\sigma - \varepsilon$ curves obtained with Material 2 specimens of distinct radii and using several initial gauge lengths: a) initial gauge length=1ϕ, a) initial gauge length=2ϕ, a) initial gauge length=12.5 mm. [23]

desired length. In [16] this issue was studied by testing 6mm-diameter specimens with increasing values of L_1. In both materials, 1 and 2, the specimen length did not seem to affect the ultimate strain as can be observed in Figure 6), that shows the results for distinct specimen lengths (L_1) using a fixed initial gauge length of 12.5 mm.

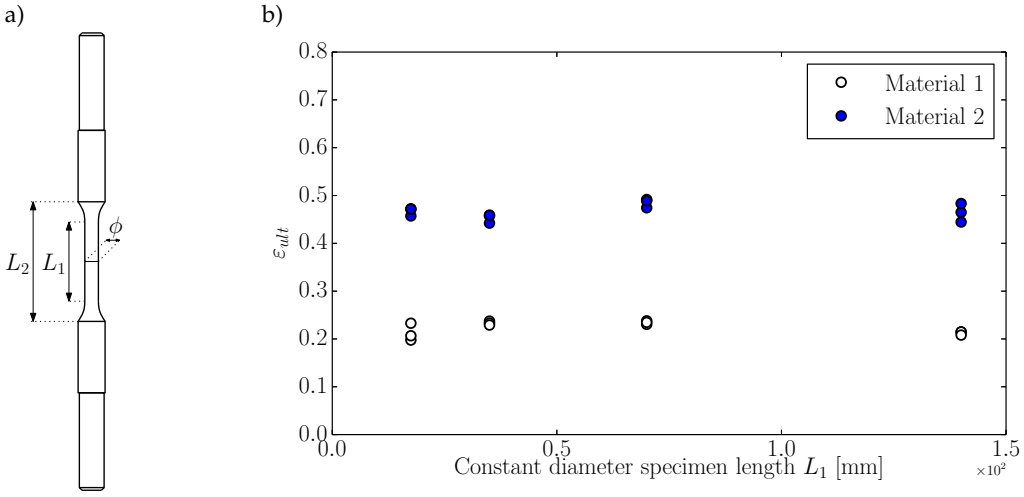

Figure 6. a) Specimen parameters for tensile tests, b) influence of the specimen length on the ultimate strain under tensile loading for an initial gauge length of 12.5 mm. [16].

2.2. Strain fields maps

One of the reasons that make DIC a powerful technique is that, differently from the conventional extensometers, which provide elongation values between only two points of the specimen, it can be used to obtain the strain maps at the surface of the specimen. Figures 7 and 8 show the longitudinal strain evolution on specimens of Materials 1 and 2, respectively; in both cases sub-figure a) represents the strain map at the maximum load instant and d) at the very last instant before failure, with b) and c) being intermediate images between a) and d).

The strain maps help to understand the differences observed when a fixed gauge length is used with distint diameter specimens. In Figures 4c) and 5c), the curves for all diameters were coincident up to the maximum load point and bifurcated later, showing smaller values of strain for smaller diameters.

The reason is that, as Figures 7 and 8 show, the strain gradient becomes greater as the tensile test progresses; therefore, if a proportional-to-the-diameter gauge length is used, the strain measured is comparable among distinct diameter specimens, proving that the necking phenomenon is proportional to the diameter, which explains why the curves in these cases are coincident beyond the maximum load point. Nevertheless, when a fixed gauge length is used, the gauge provides an average strain value in the part of the specimen that is between the selected points, therefore, in the case of smaller diameter specimens, the gauge length includes parts of the specimen relatively distant from the necking region, which results in smaller values of ε, while in the case of larger diameter specimens the gauge length includes regions that present comparatively higher strain gradients and, therefore, the average values of ε are larger. The strain gradient is higher in the case of Material 2 compared with the strain maps of Material 1, which explains why the bifurcation is more evident in Figure 5 than in Figure 4.

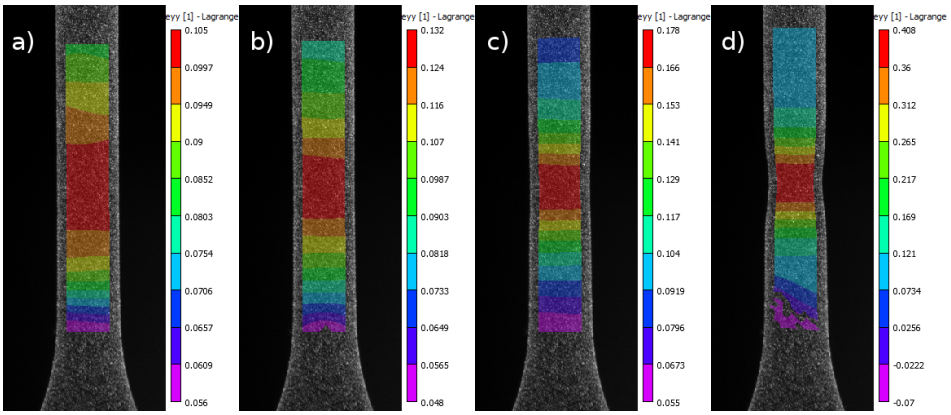

Figure 7. Evolution of the vertical strain field from the maximum load point (a) to the instant just before failure (d) for a 3-mm diameter specimen of Material 1. [23]

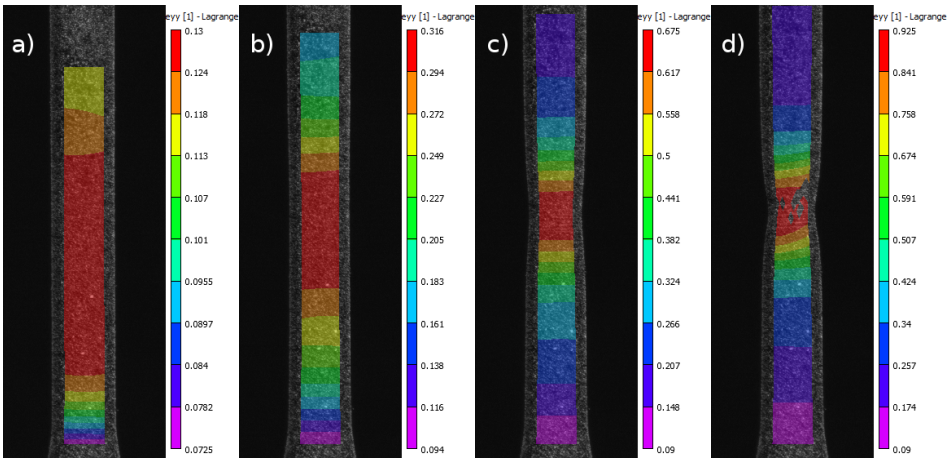

Figure 8. Evolution of the vertical strain field from the maximum load point (a) to the instant just before failure (d) for a 3-mm diameter specimen of Material 2. [23]

2.3. *Analysis of the fracture surface*

In 1966, Bluhm and Morrisey carried out an ambitious and pioneering study of the damage evolution on cylindrical bars made of three ductile metals under tensile loading [3]. To do it, they used a device (see Figure 9a) that could apply loading in a progressive manner, allowing a gradual crack propagation, and ultrasonic and metallographic techniques for identifying internal damage. In

this study they already identified several phenomena that helped to understand better the load-strain curve of a tensile test with this type of materials (see Figure 9b)):

- After necking localises, small microvoids develop, interfacial non-connected cracks at inclusions appear, as well as short intercrystalline cracks.
- Later, as strain increases, the volume of voids and cracks also increase, weakening the material matrix in the center of the necking region. Around this weakened zone, an esentially non-fractured region remains under a low hydrostatic stress state, thus being under high shear stresses that eventually lead to cracking out of the initial fracture plane, which are the so-called shear lips.

This explains the typical cup-cone fracture pattern, which would be deeply studied later by several researchers.

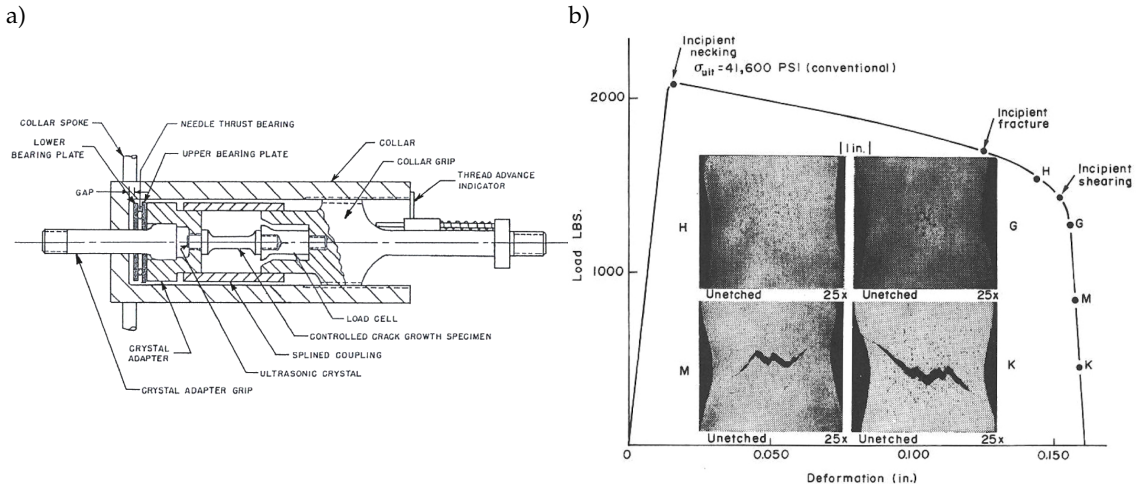

Figure 9. a) Device used by Bluhm and Morrisey to study fracture on cylindrical bars made of different metals , b) Evolution of the damage process in the necking region of a copper cylindrical specimen under tension [3]

In this section the fracture surface on both analysed patterns, type 1 (flat fracture pattern) and type 2 (cup-cone pattern), are studied by means of a scanning electronic microscope (SEM) and by analysing the geometry of both fracture surfaces for specimens of distinct diameters.

2.3.1. Fractographs

Figure 10 shows a 9 mm-diameter specimen of Material 1 observed with a SEM; the dashed circunference represents the dark area that can be observed on the fracture surface with a mere visual inspection (see Figure 1a)). The central region, which corresponds to the characteristical dark area of this pattern, presents dimples, usually related with a nucleation-growth-coalescence mechanism, while the surrounding region shows the so-called river marking related with a cleavage mechanism. In Figure 11, the analogous SEM analysis of a 9 mm-diameter specimen of Material 2 can be observed; the dashed circunference identifies the circular flat plane of the cup-cone pattern. These images show that the central region is the result of a nucleation-growth-coalescence process while the surface observed in the shear lips show a certain development of cleavage, probably mixed with nucleation-growth and coalescence of microvoids.

2.3.2. Size of the internal damage

The dark region observed in the fracture pattern of type 1 can be seen as an internal notch induced by a nucleation-growth-coalescence process developed during the loading process. Following this idea, the material behaviour would be ductile although the final failure mechanism would be triggered by a

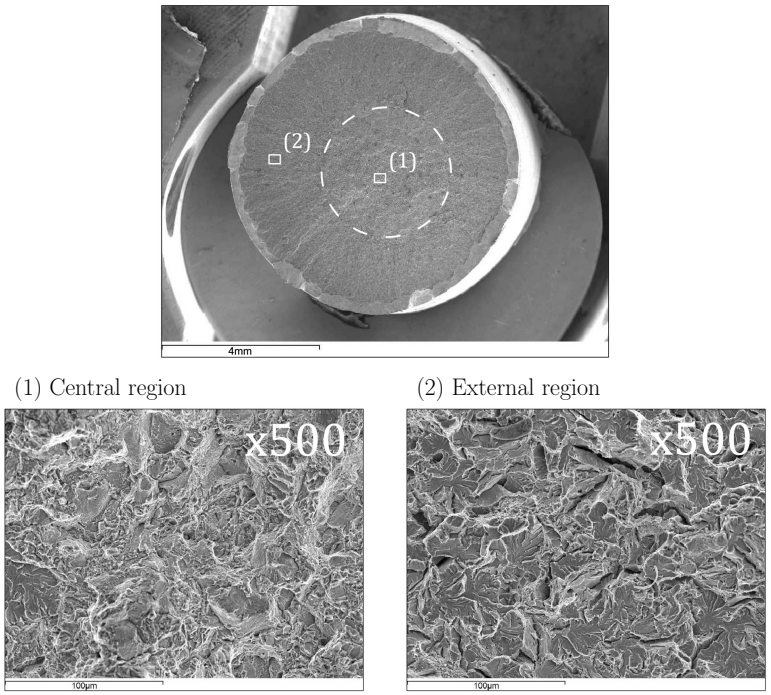

Figure 10. SEM analysis on the fracture surface of a 9 mm. diameter specimen of Material 1. [16]

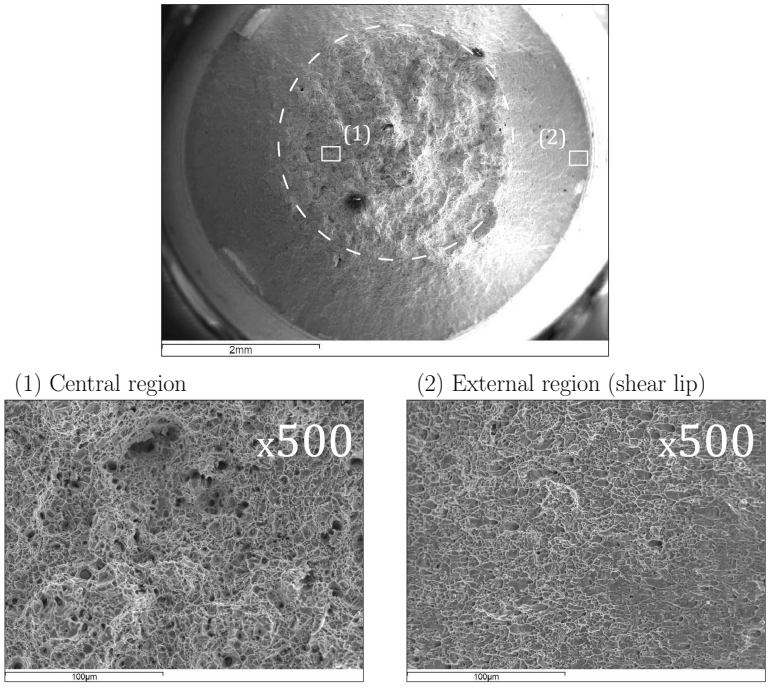

Figure 11. SEM analysis on the fracture surface of a 9 mm. diameter specimen of Material 2. [16]

quasi-brittle behaviour, such quasi-brittle behaviour is explained by the presence of the dark region which acts as an internal crack that, once large enough, concentrates stresses around a very especific region of the damage cross-section and leads to a brittle fracture process at the very end of the test.

The area of the dark region observed in fracture surfaces of Material 1 does not seem to be proportional to the specimen cross-section at first sight. If the dark region diameter ($2r$) and the minimum diameter of the specimen at necking ($2R_{min}$) are measured, the evolution of r/R_{min} is observed to decrease with the specimen size, as shown in Figure 12a). When the same analysis was carried out on specimens of Material 2, considering $2r$ as the diameter of the flat circular region of the cup-cone surface, the proportion r/R_{min} remained constant for any specimen size (see Figure 12b)).

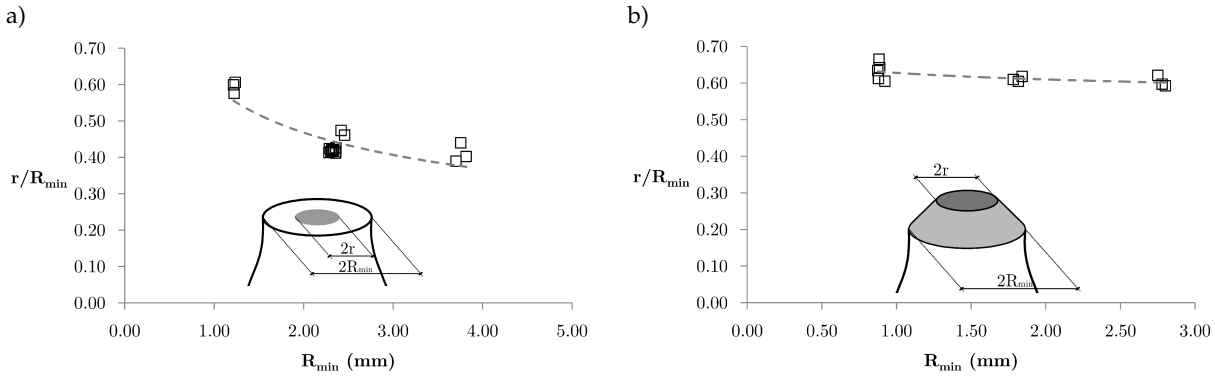

Figure 12. r/R_{min} relations experimentally obtained on specimens with diameters of 3, 6 and 9 mm for a) Material 1 , b) Material 2 [23].

Under the aforementioned approach, the final fracture process can be approached by using expressions based on LEFM for the case of Material 1, which are valid for brittle materials. Thus, considering that the fracture process can be studied as the fracture of a cylindrical specimen with an internal circular crack, the formula provided by Guinea, Rojo and Elices [24,25] can be used:

$$\frac{K_I}{K_0} = 1 + \sum_{i=1}^{5} C_{i0} \left(\frac{r}{R}\right)^{\frac{2i+1}{2}} + \sum_{i=1}^{3} \left\{ \ln\left[1 + \left(\frac{r}{R}\right)^{2i}\right] \cdot \left[C_{i1} \ln^2\left(\frac{b}{R}\frac{r}{R}\right) + \frac{C_{i2}}{\sqrt{\frac{b}{R}\frac{r}{R}}}\right] \right\} \quad (1)$$

where the reference stress intensity factor K_0 is:

$$K_0 = \frac{2}{\pi} \cdot \sigma \sqrt{\pi r}$$

where (see Figure 13a)):

- K_I is the stress intensity factor.
- b stands for the smaller distance between the crack boundary and the specimen boundary.
- r is the internal crack radius.
- R is the specimen radius.
- σ is the tensile stress away from the fracture zone.
- C_i are the coefficients defined in Table 2.

Table 2. C_i coefficients used in the Guinea-Rojo-Elices expression for the computation of K_{Ic} in cylindrical fibers under tension with eccentric internal crack perpendicular to the specimen axis [24].

	C_{i0}	C_{i1}	C_{i2}
i=1	0,01242	-0,3097	1,185
i=2	-6,388	1,547	-3,723
i=3	16,89	-0,8769	2,628
i=4	-9,838	—	—
i=5	-1,228	—	—

The value of the fracture toughness K_{Ic} can be obtained by means of a three-point bending test, described by the ASTM E 399-90 [26]. Therefore, once K_{Ic} is known, for each value of R_{min}, the value of r that satisfies (1) can be easily obtained. Figure 13 compares the values of proportion r/R_{min} obtained experimentally and those obtained with (1), thus based on the LEFM. These results show that the experimental values decrease with the specimen size, which agrees with the tendency predicted by the LEFM, which supports the hypothesis of an eventual fracture driven by brittle mechanisms. In contrast to these results, the almost constant r/R_{min} ratio exhibited by Material 2 specimens suggest a final failure not ruled by LEFM considerations.

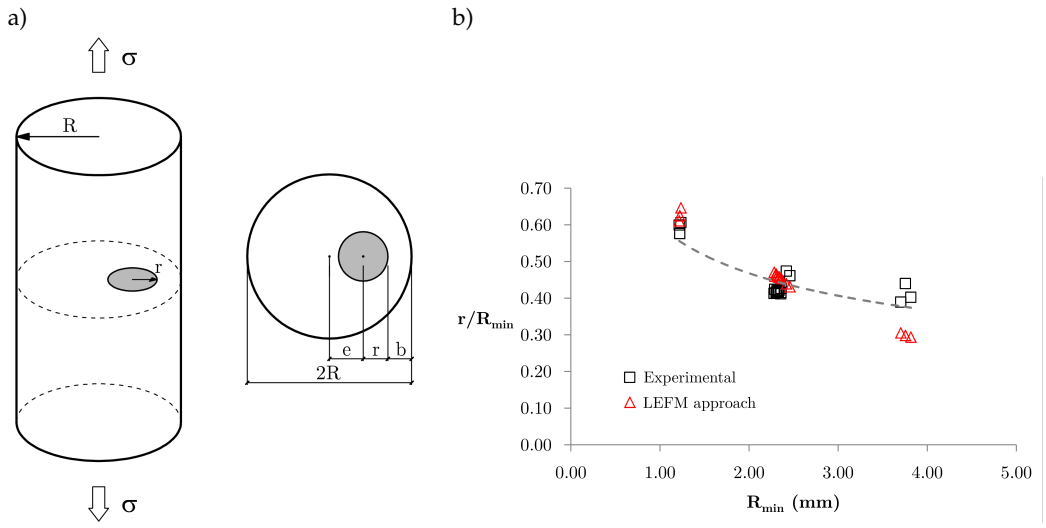

Figure 13. a) Parameters used in the expression of Guinea, Rojo and Elices [24], b) r/R_{min} values obtained with the expression based on the LEFM compared with the experimental results [23].

2.4. Evolution of damage

All the works mentioned before seem to confirm that, in the case of fracture pattern 1, damage initiates inside the specimen producing something similar to an internal defect that eventually leads to a brittle fracture process, but there is no evidence of when this damage begins to develop. In this section two approaches are described which have helped to identify that the damage develops in the very late stages of the tensile test.

2.4.1. Tests on embrittled specimens by means of liquid nitrogen

The stress-strain diagram of Material 1 is very repetitive, so a tensile test can be carried out to a certain desired strain level with notable precision. In [15] four 6 mm specimens of this material were tested up to increasing strain levels that ranged from the maximum load instant up to fracture, with the highest of them being very close to failure. Each specimen was then unloaded and tested again until failure at extremely low temperatures in order to induce an embrittled fracture that would

allow identification of the previously developed internal damage. Figure 14a) shows the experimental setup; the specimens where submerged into liquid nitrogen and the test was carried out with a rapid displacement of the clamping jaws once the temperature, measured with a thermo-couple, was lower than -100^{o}C.

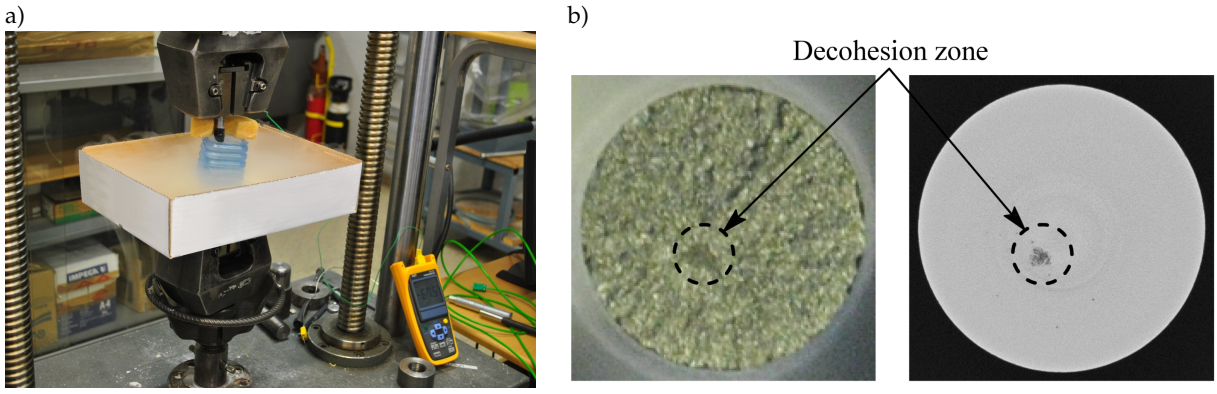

Figure 14. a) Experimental setup for the test on specimens embrittled with liquid nitrogen, b) Comparison between the visual inspection after failure and the internal damage observed with X-ray computed tomography before failure [16].

This procedure proved to be efficient and allowed to identify an internal damage only in the specimen tested at the more advanced strain level. In addition, this specimen was also analysed by X-ray computed tomography (XRCT) before the embrittled test. The tomographic image obtained also identified the internal damage that could be observed after carrying out the embrittled test. Figure 14b) shows both results compared, which allows considering this region as the beginning of the dark region that can be usually observed in this fracture pattern, which can be considered as an internal decohesion process.

2.4.2. Tests analysed with X-ray computed tomography

As seen before, XRCT allows identifying internal damage in the specimens, so a more detailed study of the damage evolution was done using this technique on both materials. For each of them, a 3 mm diameter sample was tested up to a certain strain level, then unloaded and analysed with XRCT. Later on, the same sample was retested up to a higher strain level, unloaded and analysed with XRCT again. This process was repeated increasing the strain level until the sample was broken. Figures 15 and 16 show the tomographic images obtained for both materials at each of the analysed strain levels.

In the case of Material 1, the matrix looks compact and homogeneous in the intact material and, as strain increases after maximum loading, the formation of small voids can be observed. Interestingly, some of these voids are formed following a longitudinal direction, which could be due to the manufacturing process. In this case, voids only coalesce at the very last stage of the test, corresponding to step 4 in the figure, in agreement with the behaviour observed in the 6 mm samples analysed with liquid nitrogen. Here, again, the decohesion process is identified, which will result in the dark region observed on the fracture surface of this material.

In the case of Material 2, the initial tomography, obtained with the intact specimen before testing, already shows a very heterogeneous matrix, with inclusions that are also lined up in the longitudinal direction, probably as a result of the manufacturing process. As strain increases, damage seems to develop all around the necking region.

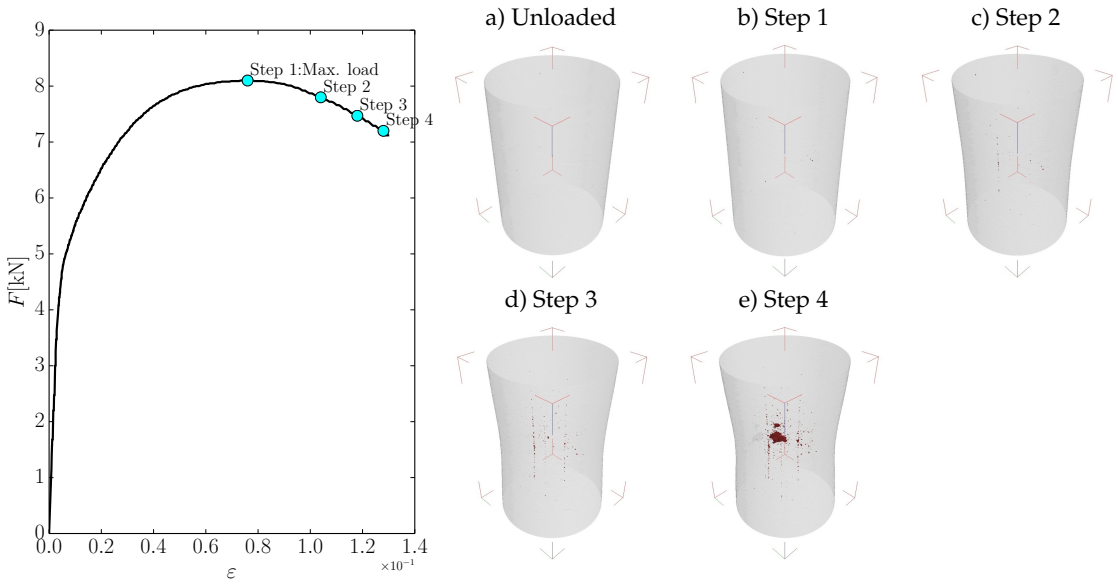

Figure 15. Evolution of internal damage on a 3-mm diameter specimen of Material 1. Images obtained by means of X-ray computed tomography [16]

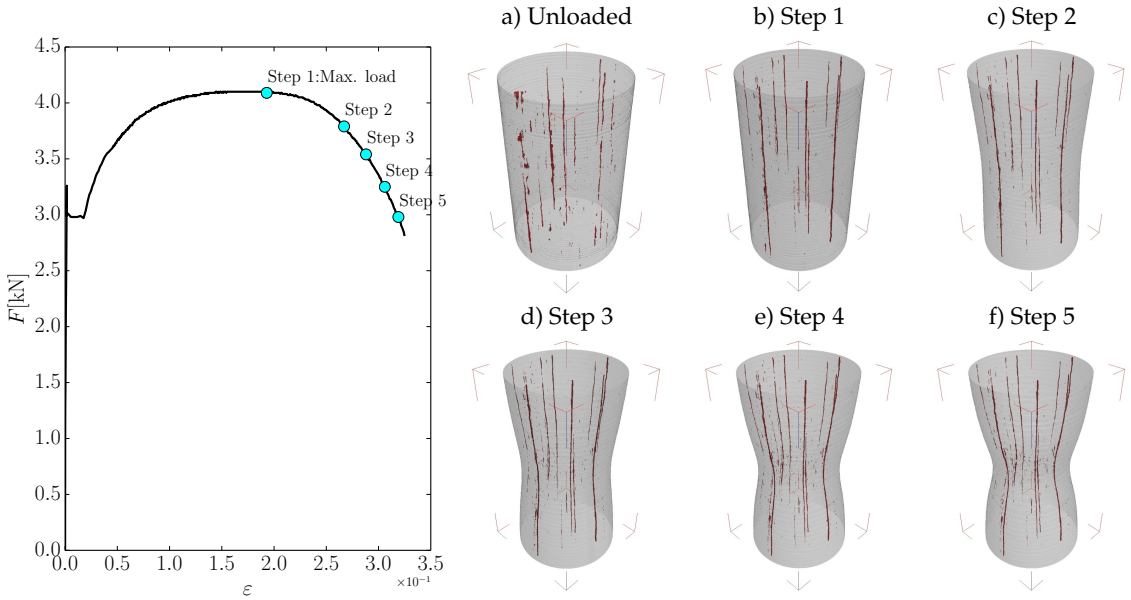

Figure 16. Evolution of internal damage on a 3-mm diameter specimen of Material 2. Images obtained by means of X-ray computed tomography [16]

2.5. *Influence of stress triaxiality on ductile fracture*

Stress triaxiality is defined as the ratio $\sigma_H/\bar{\sigma}$, with σ_H being the hydrostatic pressure and $\bar{\sigma}$ the Von Mises equivalent stress. This value provides information of how balanced or unbalanced the principal stresses σ_1, σ_2 and σ_3 are.

Mirza et al. [27] studied the influence of the stress triaxiality using copper specimens; they performed tensile tests stopped before failure in order to, once unloaded, polish them to observe the matrix inside the specimen and identify internal damage. They conluded that the stress triaxility plays a paramount role on how the nucleation-growth-coalescence mechanism develops. In this sense, Toribio et al. [28–30] also studied the influence of triaxiality using notched specimens to induce distinct triaxiality states in the fracture process.

The main material models developed until the mid-nineties included the stress triaxiality in their formulation in an implicit way, for example, by means of parameters p and q in the Gurson model [31] and by means of the Bridgman equations [32] in the Johnson-Cook [33] model.

The works by Bao and Wierzbicki [34–36] help to understand how this issue affects fracture on metallic specimens. They conducted a large experimental programme with alluminum specimens covering a wide range of triaxiality states, from compression to multiaxial tension. Figure 17 presents one of their most relevant results, a diagram that shows how the ultimate strain is dependent on the stress triaxiality. One of their main conclusions is that the influence of the stress triaxiality cannot be modelled by a monotonic function, as other authors had done in the past [33,37], but three distinct regions must be considered; in each region the governing fracture mechanisms are different:

- Zone I: low triaxialities, where fracture is mainly due to shearing.
- Zone II: medium triaxialities, where fracture is the result of a combination of shearing and the nucleation-growth-coalescence mechanism.
- Zone III: high triaxialities, where the nucleation-growth-coalescence mechanism drives fracture.

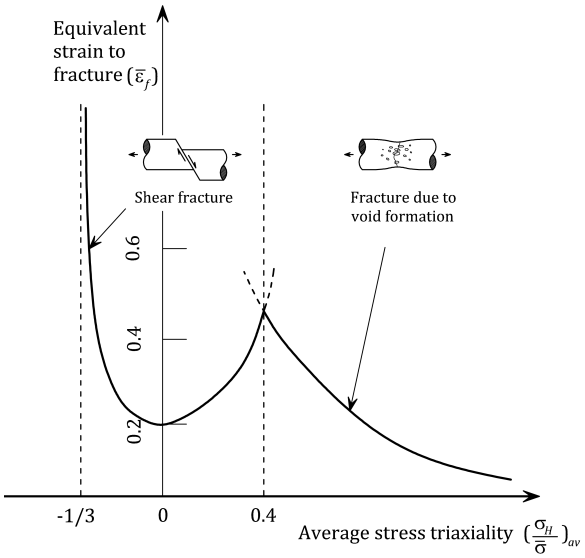

Figure 17. Influence of stress triaxiality on the equivalent strain to fracture (adapted from [35])

2.5.1. The Lode angle

In the last years, several models and approaches have been based on the so-called Lode angle [38]. If working with the principal stresses coordinate system (σ_1, σ_2, σ_3), any stress state can be represented by means of the Haigh-Westergaard coordinates ξ, ρ and θ:

$$\begin{aligned} \xi &= \frac{I_1}{\sqrt{3}} = \sqrt{3}p \\ \rho &= \sqrt{2J_2} \\ \theta &= \frac{1}{3}\cos^{-1}\left(\frac{3\sqrt{3}}{2}\frac{J_3}{J_2^{3/2}}\right) \end{aligned}$$

where I_1 is the first invariant of the Cauchy stress tensor, J_2 and J_3 stand for the invariants of the stress deviator tensor and p for the hydrostatic stress. Parameter θ is usually referred to as the Lode angle.

In [39], a new approach to ductile fracture was proposed by using the Lode parameter, which in combination with the stress triaxiality is considered as fundamental to identify the fracture direction in ductile materials. In that work, Zhang et al. confirmed that the stress triaxiality is not enough to define the fracture behaviour of a ductile material and another value, in this case the Lode parameter, must be used. Since then, many authors have used the Lode parameter in ductile fracture models. For instance, Wue and Wierzbicki [40] proposed a model where the damage criterion was based on the stress triaxiality and a parameter related to the Lode angle, Bai and Wierzbicki [41] proposed later a ductile fracture model based on the stress triaxiality and the Lode parameter, and Erice and Gálvez [42,43] developed a coupled elastoplastic damage model with a failure criterion dependent on the Lode angle. The importance of the Lode angle in ductile fracture processes was confirmed by Mirone and Corallo [44], who studied its influence on fracture of different metals, and Barsoum and Faleskog [7,8,45], who based their work on the mechanisms of growth and coalescence of microvoids, concluded that the Lode parameter has a high influence on the nucleation and growth of voids but not much if the triaxiality is high, when it is the stress triaxiality which drives the fracture process.

3. Numerical models

3.1. Models usually employed with metals

There are a number of material models that are currently used for simulating fracture in metals. The election of the model depends on the user's needs, for example, if the parameters that want to be considered in the fracture process involve strain rate, temperature or pressure, the Johnson-Cook model that will be briefly described later, would be a good choice.

If we consider the coupling of the elastoplastic behaviour and the fracture behaviour, we can divide these models in coupled and uncoupled. In the following lines, a brief overview of the main models used for reproducing fracture in metals is provided. Some of these formulations are the result of an analytical treatment of the problem and others are based on experimental adjustments of the problem. In any case, the reader will find that all of them include triaxiality as a key factor in the ductile fracture process and that some of them also include the Lode parameter.

After this overview, a model developed by the authors is described. This model is based on the cohesive crack concept and its formulation is affected by triaxiality, showing to reproduce reasonably well the fracture behaviour of Material 1.

3.1.1. Uncoupled models

In these models, damage process does not affect the elastoplastic constitutive equations. A damage parameter must be defined, usually dependent on the plastic strain accumulation.

These models are usually phenomenological and, since the elastoplastic and failure criteria can be observed independently, are also usuallly easier to calibrate. Stress is not affected by a progressive deterioration process, which lead to rather an abrupt failure behaviour. Some fracture patterns, such as the cup-cone shape, cannot usually modelled by this type of formulations.

Johnson-Cook model

The Johnson-Cook model [33,46] is very extended when strain rate and thermal softening or pressure are important factors to be considered in the fracture process, i.e. ballistic applications [47–51] and blast loadings [52–55]. This model defines a damage parameter D expressed by (2), where $\Delta\bar{\varepsilon}_p$ is the equivalent plastic strain rate and $\bar{\varepsilon}_p^R$ the equivalent plastic strain to failure, that is dependent on the strain rate, temperature and pressure, as expression (3) shows. In this expression D_1, D_2, D_3, D_4 and D_5 are material constants that must be callibrated, σ^* stands for the stress triaxiality, $\dot{\bar{\varepsilon}}_p^*$ for a dimensionless plastic strain rate ($\dot{\bar{\varepsilon}}_p^* = \dot{\bar{\varepsilon}}_p/\dot{\varepsilon}_0$, with $\dot{\varepsilon}_0$ being a reference plastic strain rate) and T^* takes into account the effect of temperature.

$$D = \sum \frac{\Delta\bar{\varepsilon}_p}{\bar{\varepsilon}_p^R} \tag{2}$$

$$\bar{\varepsilon}_p^R = \left[D_1 + D_2 \exp\left(D_3\sigma^*\right)\right]\left[1 + D_4 \ln \dot{\bar{\varepsilon}}_p^*\right]\left[1 + D_5 T^*\right] \tag{3}$$

Wilkins' et al. model

Wilkins' et al. material model [56] includes a scalar parameter A that plays a similar role as the Lode parameter in later models and depends on the principal deviatoric stresses (s_1, s_2, s_3) by means of expression (4).

$$A = \max\left(\frac{s_2}{s_3}, \frac{s_2}{s_1}\right) \tag{4}$$

Then, the hardening function reads:

$$Y = Y_T(\bar{\varepsilon}_p)A^\lambda + Y_S(\bar{\varepsilon}_p)(1 - A^\lambda) \tag{5}$$

where Y_T is the equivalent strain hardening function for uniaxial tension/compression, Y_S the equivalent strain hardending function for pure shear/torsion and $\bar{\varepsilon}_p$ the equivalent plastic strain. The parameter λ is a material constant and must be experimentally adjusted.

The damage is dependent on the history of the plastic strain and its evolution depends on the plastic strain rate and two separate weighting functions (see expression (6)), one depending on the hydrostatic pressure (p) and another depending on the parameter A.

$$\dot{D} = w_1(p)w_2(A)\dot{\bar{\varepsilon}}_p \tag{6}$$

Bai-Wierzbicki model

The model proposed by Bai and Wierzbicki [41] explicitly introduces triaxiality dependence in the hardening function, expressed by (7), where $\bar{\sigma}(\bar{\varepsilon}_p)$ represents the equivalent strain hardening function for a reference test, σ_0^* the reference value of the stress triaxiality in the reference test, $\bar{\varepsilon}_p$ the equivalent plastic strain, σ^* the stress triaxiality, c_{σ^*}, c_θ^s and m are material constants and γ and c_θ^{ax} parameters dependent on the Lode angle θ.

$$\phi = \bar{\sigma}(\bar{\varepsilon}_p)\left[1 - c_{\sigma^*}(\sigma^* - \sigma_0^*)\right]\left[c_\theta^s + (c_\theta^{ax} - c_\theta^s)\left(\gamma - \frac{\gamma^{m+1}}{m+1}\right)\right] \tag{7}$$

The damage accumulation is the same as in the Johnson-Cook model and thus depends on five material constants that must be callibrated.

3.1.2. Coupled models

These models are usually based on micro-mechanical observations and the elastoplastic behaviour is affected by the degradation process that leads to eventual failure. Because of their coupled nature,

their callibration is usually more tedious than in the case of uncoupled models, but are quite often selected by the scientific community due to their solid framework usually based on micromechanics.

Lemaitre's model

In this model [57,58], strain is obtained by expression (8), where D is a scalar variable that ranges from 0 to 1 and describes how damaged the material is, $\boldsymbol{C}$ is the elastic fourth-order tensor and $(\boldsymbol{\varepsilon} - \boldsymbol{\varepsilon}_p)$ the elastic strain.

$$\boldsymbol{\sigma} = (1 - D)\boldsymbol{C} : (\boldsymbol{\varepsilon} - \boldsymbol{\varepsilon}_p) \tag{8}$$

The yield function is defined by (9), where $\bar{\sigma}$ is von Mises equivalent stress and σ_y is the isotropic hardening rule, dependent on a hardening variable r.

$$\phi = \frac{\bar{\sigma}}{(1 - D)} - \sigma_y(r) \tag{9}$$

Damage evolution is ruled by an expression that depends on the energy release rate, defined by (10).

$$Y = \frac{\bar{\sigma}^2}{2E(1 - D)^2}\left[\frac{2}{3}(1 + \nu) + 3(1 - 2\nu)(\sigma^*)^2\right] \tag{10}$$

where E and ν are the material elastic parameters and σ^* the stress triaxiality.

Xue-Wierzbicki model

This model [59,60] couples damage and plasticity by means of expression (11), which resembles the expression (8), from Lemaitre's model. β is a material constant that must be callibrated using the matrix material stress-strain curve.

$$\boldsymbol{\sigma} = (1 - D^\beta)\boldsymbol{C} : (\boldsymbol{\varepsilon} - \boldsymbol{\varepsilon}_p) \tag{11}$$

The yield condition is defined by (12), where σ_M represents the yield strength of the matrix material and is a function of the plastic strain ε_p.

$$\phi = \bar{\sigma}^2 - \left[(1 - D^\beta)\sigma_M\right]^2 \tag{12}$$

Damage evolves according to expression (13), where m is a material constant and $\bar{\varepsilon}_p^f$ is the fracture strain from monotonic loading, which depends on the hydrostatic pressure p and the Lode angle θ.

$$\dot{D} = m\left[\frac{\bar{\varepsilon}_p}{\bar{\varepsilon}_p^f(p,\theta)}\right]^{(m-1)}\frac{1}{\bar{\varepsilon}_p^f(p,\theta)}\dot{\bar{\varepsilon}_p} \tag{13}$$

Modified Johnson-Cook model

This model was proposed by Borvik et al. [61] and, based on the uncoupled Johnson-Cook model, reformulated as a coupled version. In this formulation, the strain rate is composed as the sum of three strain rates: elastic, plastic and thermally induced:

$$\dot{\varepsilon} = \dot{\varepsilon}^e + \dot{\varepsilon}^p + \dot{\varepsilon}^t$$

The stress tensor rate is defined by (14):

$$\dot{\boldsymbol{\sigma}} = (1 - D)\boldsymbol{C} : \dot{\boldsymbol{\varepsilon}}^e - \frac{\dot{D}}{(1 - D)}\boldsymbol{\sigma} \tag{14}$$

where $\boldsymbol{C}$ is the fourth-order elastic tensor and $\dot{D}$ accounts for the damage evolution.

As in the original Johnson-Cook model, the damage evolution is defined as:

$$\dot{D} = \frac{\dot{\bar{\varepsilon}}_p}{\bar{\varepsilon}_p^R} \tag{15}$$

The proposed expression for the equivalent plastic strain to fracture $\bar{\varepsilon}_p^R$, (16), is similar to that in the original Johnson-Cook model, although a different influence of the strain rate is considered.

$$\bar{\varepsilon}_p^R = \left[D_1 + D_2 \exp\left(D_3 \sigma^*\right)\right] \left[1 + \dot{\bar{\varepsilon}}_p^*\right]^{D_4} \left[1 + D_5 T^*\right] \tag{16}$$

Gurson-like models

The Gurson-Tvergaard-Needleman (GTN) model is one of the most successful when fracture in metals is to be modelled. The seminal model was proposed by Gurson in 1977 [31], who based its formulation on the growth of a spherical void inside a material matrix, studied earlier by Rice and Tracey [62]. The model developed by Gurson could predict the loss of strength due to the nucleation and growth mechanisms, but not the total material loss of strength. Tvergaard and Needleman [4] modified the model including a failure criterion and were able to reproduce the typical cup-cone fracture. The yield function is defined by (17), where f^* represents the voids volume fraction of the material, which introduces the failure criterion based on the void volume at the beginning of the coalescence mechanism and the voids volume when there is a total loss of strength; q_1, q_2 and q_3 are model parameters that, according to Tvergaard and Needleman, can be considered to be around 1.5, 1.0 and 2.25, respectively.

$$\phi = \left(\frac{\bar{\sigma}}{\sigma_y}\right)^2 + 2q_1 f^* \cosh\left(-q_2 \frac{3\sigma_H}{2\sigma_y}\right) - \left(1 + q_3 f^{*2}\right) \tag{17}$$

This model introduces the effect of triaxiality by means of the hydrostatic stress σ_H and the von Mises equivalent stress $\bar{\sigma}$. Since its appearance, it has been often used to study fracture in ductile materials and is still a referent model in the field. The model is able to reproduce ductile fracture in many materials [27,63,64], has been compared with other models proving to be very precise [65] and has even been used to study cases of ductile-brittle damage transition [66].

Many researchers have paid attention to this model and have adjusted its formulation to make it usable in other situations. For example, Hao and Brocks [67] proposed a variation that included the influence of temperature, Steglich et al. [68] combined the GTN and cohesive models to reproduce fracture in particle-reinforced metals, Zhang [39] modified the model formulation to reproduce coalescence in terms of the plastic limit by Thomason. In its original formulation, the GTN model is limited, since in cases of null hydrostatic pressure, damage does not develop; to solve this problem, Nahson and Hutchinson [69] proposed a modification that took into account cases of pure shear and cases where the hydrostatic pressure was very low; nevertheless, it was later proved that this version overestimated damage in cases with high triaxialities [70]. Later versions of the model by several authors can be found [64,71–74], some even including the Lode angle in their formulation [75,76].

In spite of the wide acceptance and usage of this model, it has also been found to present some drawbacks, mainly two: the parameters that feed the model cannot be experimentally measured, since they refer to voids volume fractions that cannot be quantified by experimental procedures, and distinct set of callibrated parameters can be found to be valid for the same material [68].

3.2. Triaxiality-dependent cohesive model

The cohesive crack concept was proposed in the seventies by Hillerborg [77], based on the work by Dugdale and Barenblatt [78], and was applied in the framework of Linear Elastic Fracture Mechanics (LEFM). Many models have appeared since then and have based the material damage on a softening

function that is defined by only two parameters, the tensile strength f_t and the fracture energy G_f. The main advantages of these models are their simplicity and their easy callibration, which can be done by standardised experimental tests [79,80], ensuring an objective procedure of callibrating and modelling the fracture process. Besides this, they can be combined with any material model for the continuum, including those discussed in the previous sections. For further details on this numerical model, the reader is referred to [81] and [82].

This numerical approach has been used by many researchers since its appearance and has allowed implementing interface cohesive elements for quasi-brittle materials under mode I or under the combination of modes I, II and III loading [83–89], smeared crack models [90–94] and embedded crack models [95–101].

Although the cohesive zone model is in principle valid in quasi-brittle materials, such as concrete or cement-based materials, it has also been used in metals. Siegmund and Brocks [102] used a cohesive crack model to study the crack growth in elastic-plastic materials and Scheider and Brocks [6,103] used a cohesive model to simulate the cup-cone fracture and even made it dependent on triaxiality.

In [15], fracture pattern 2 was modelled by means of a cohesive zone model where the cohesive parameters f_t and G_f were dependent on the stress triaxiality. To do this, an interface element reproduced the fracture behaviour, which was fed by the stress triaxiality values of the adjacent element (see Figure 18). In this case, since the fracture of a metal is reproduced, a rectangular-shaped softening function is recommended [78]; given that for numerical reasons a rectangular shape induces many convergence problems, a parabolic shape that resembles a rectangular behaviour is used.

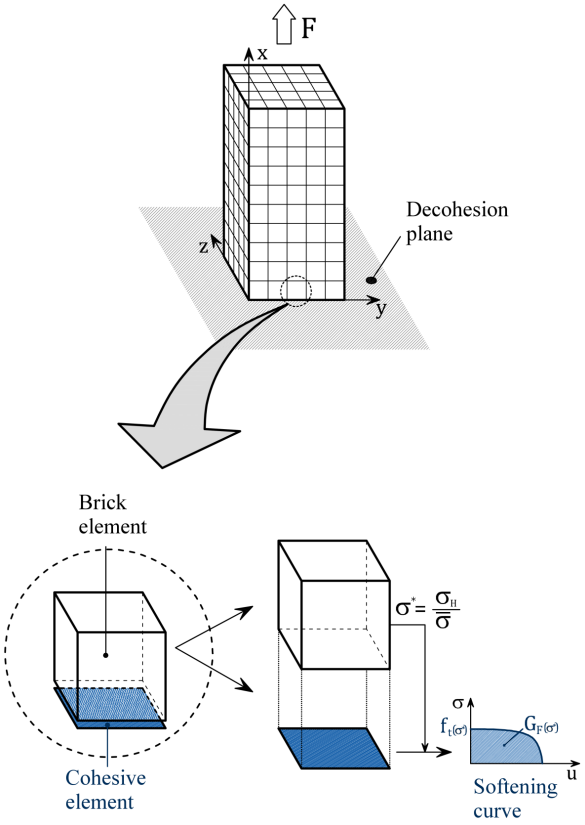

Figure 18. General graphical representation of the triaxiality-dependent cohesive zone interface element [15].

This model is fed by f_t and G_f values that can be obtained by standardised tests [26,104] and reproduces reasonably well the decohesive process assumed in the center of the specimens that leads to the dark region that can be observed in the fracture surface. As can be observed in Figure 19, when this

model is applied for modelling fracture in a cylindrical specimen of Material 1, fracture initiates in the center of the specimen, unloading that part of the eventual fracture plane and, therefore, transfering a stress increment to the surrounding region. As strain increases, this decohesive process propagates from inside to outside.

This model provides reasonably good agreement with the experimental results, although it does not provide a fracture criterion for the ductile-brittle transition observed in this type of fracture (see Figure 1a)).

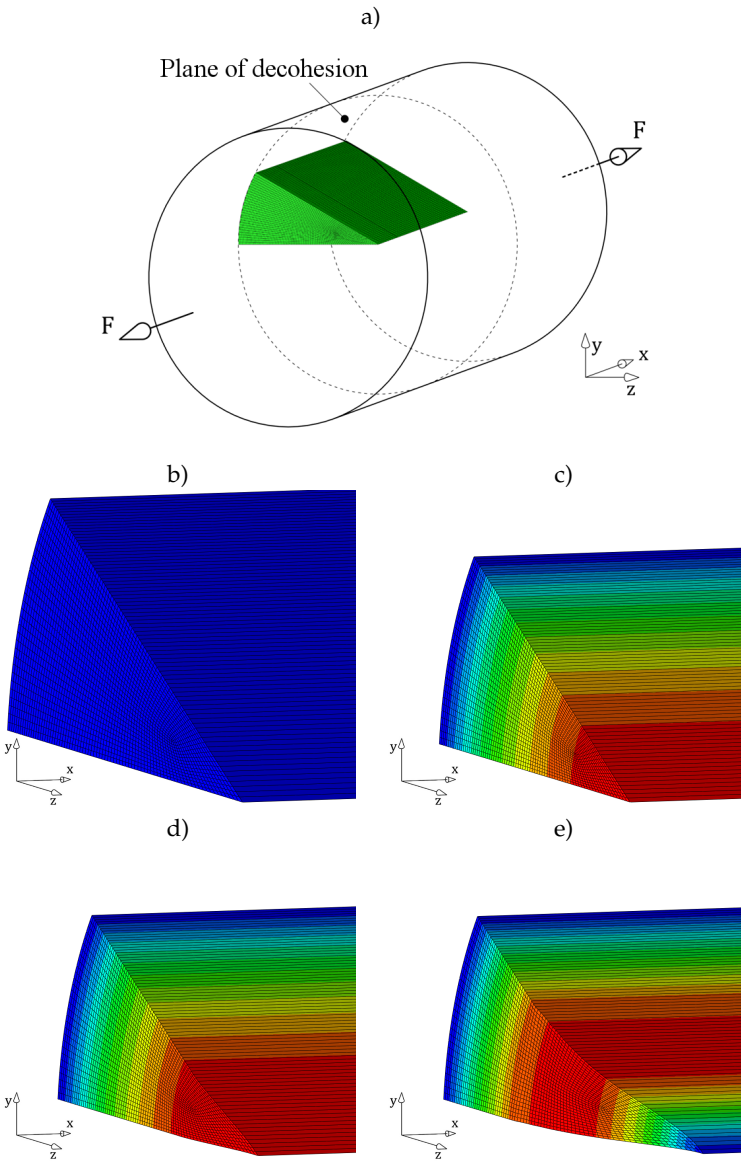

Figure 19. Evolution of decohesion at the fracture plane: a) grid used to simulate the fracture process, b) fracture plane before loading, c) stress concentrates in the center as loading is applied, d) decohesion begins, e) the decohesive process propagates from inside to outside. [15]

The similar approach has been successfully employed later [105] with gray cast iron, but instead of by using interface elements, by means of crack-embedded elements.

4. Final comments

In this paper, a review on the late advances made on the study of the two more usual fracture patterns observed on construction steels has been carried out, paying special attention to the material behaviour after maximum loading and the analysis of the fracture surfaces.

From the experimental point of view, although the ultimate strain values are usually neglected in practice, the experimental results carried out using a digital image correlation system, have proved to be very repetitive and independent from the specimen radius and length. Hence, in principle they could be used as reliable data if certain considerations are taken into account:

- If specimens of different radii are to be compared, a proportional-to-the-radius initial gauge length should be considered.

- The reference gauge length must be centered with the eventual fracture plane, otherwise the strain gradient would affect the measurements; this can be accomplished by using a digital image correlation system and not with conventional extensometers.

X-ray computed tomography allows identifying internal damage in steel, at least if thin enough specimens are used. This technique has helped to identify the internal damage evolution during a tensile test in the necking region. In the case of Material 1, which corresponds to an eutectoid steel used for manufacturing prestressing wires, the internal damage that eventually leads to a brittle fracture mechanism can be identified.

The study of the fracture surfaces geommetries suggest that the fracture mechanisms of both analysed materials differ notably, not only for their final shape (cup-cone pattern and flat surface with internal dark circular region), but also because in the case of Material 1, this geometry proves not to be proportional to the specimen diameter, while in the case of Material 2, this proportionality can be observed.

A brief overview on the most extended numerical models for ductile materials has confirmed that the triaxiality dependence must always be considered in this type of fracture and, in many cases, also the influence of the Lode angle. The use of a cohesive crack formulation, has proved to provide reasonably good results even for metallic materials; this approach has been used by some researchers in the last years, including an application by the authors by using interface elements with the finite element method.

All the mentioned information can help to understand and support studying the behaviour of distinct steels beyond their maximum bearing capacity, which is usually neglected and considered unreliable. The works presented seem to point out in a different direction, since if the experimental work is carefully carried out, results seem to be pretty repetitive and reliable. A better understanding of this issue can help to extend the usage of these materials beyond their current limits, which is considered of interest, since the last part of the stress-strain diagram, between maximum loading and failure, is the main responsible for the energy absorbed by the material before collapsing. This could help to design better strategies in projected structures that could lead to higher structural safety conditions.

Acknowledgments: The authors gratefully acknowledge the financial support provided for this research by the Ministry of Economy and Competitiveness of Spain by means of the Research Fund Project BIA 2016-78742-C2-2-R.

Author Contributions: Jaime C. Gálvez and J. M. Atienza conceived and designed the experiments; Fernando Suárez performed the experiments; Fernando Suárez, David A. Cendón and Jaime C. Gálvez analyzed the data; Fernando Suárez and David A. Cendón carried out the numerical modelling; Fernando Suárez wrote the paper.

Conflicts of Interest: The authors declare no conflict of interest. The founding sponsors had no role in the design of the study; in the collection, analyses, or interpretation of data; in the writing of the manuscript, and in the decision to publish the results.

References

1. ISO, E. 6892-1. Metallic materials-Tensile testing-Part 1: Method of test at room temperature. *International Organization for Standardization* **2009**.
2. ISO, E. 15630-1. Steel for the Reinforcement and Prestressing of Concrete-Test Methods-Part 1. *International Organization for Standardization* **2002**.
3. Bluhm, J.I.; Morrissey, R.J. *Fracture in a Tensile Specimen*; Defense Technical Information Center, 1966.
4. Tvergaard, V.; Needleman, A. Analysis of the cup-cone fracture in a round tensile bar. *Acta Metallurgica* **1984**, *32*, 157 – 169.
5. Besson, J.; Steglich, D.; Brocks, W. Modeling of crack growth in round bars and plane strain specimens. *International Journal of Solids and Structures* **2001**, *38*, 8259 – 8284.
6. Scheider, I.; Brocks, W. Simulation of cup-cone fracture using the cohesive model. *Engineering Fracture Mechanics* **2003**, *70*, 1943 – 1961.
7. Barsoum, I.; Faleskog, J. Rupture mechanisms in combined tension and shear — Micromechanics. *International Journal of Solids and Structures* **2007**, *44*, 5481 – 5498.
8. Barsoum, I.; Faleskog, J. Rupture mechanisms in combined tension and shear — Experiments. *International Journal of Solids and Structures* **2007**, *44*, 1768 – 1786.
9. Huespe, A.E.; Needleman, A.; Oliver, J.; Sánchez, P.J. A finite thickness band method for ductile fracture analysis. *International Journal of Plasticity* **2009**, *25*, 2349 – 2365.
10. Huespe, A.E.; Needleman, A.; Oliver, J.; Sánchez, P.J. A finite strain, finite band method for modeling ductile fracture. *International Journal of Plasticity* **2012**, *28*, 53 – 69.
11. Hutchinson, J.W.; Tvergaard, V. Shear band formation in plane strain. *International Journal of Solids and Structures* **1981**, *17*, 451 – 470.
12. Ayaso, J.; González, B.; Matos, J.C.; Vergara, D.; Lorenzo, M.; Toribio, J. Análisis fractográfico cuantitativo del comportamiento en fractura de aceros perlíticos progresivamente trefilados. *Anales de Mecánica de la Fractura* **2005**, pp. 128 – 133.
13. González, B.; Matos, J.C.; Toribio, J. Relación microestructura-propiedades mecánicas en acero perlítico progresivamente trefilado. *Anales de Mecánica de la Fractura* **2009**, *1*, 142 – 147.
14. Rodríguez, R.; Toribio, J.; Ayaso, F.J. Defectos microestructurales que gobiernan la fractura anisótropa en aceros fuertemente trefilados. *Anales de Mecánica de la Fractura* **2009**, *1*, 148 – 153.
15. Suárez, F.; Gálvez, J.C.; Cendón, D.A.; Atienza, J.M. Fracture of eutectoid steel bars under tensile loading: Experimental results and numerical simulation. *Engineering Fracture Mechanics* **2016**, *158*, 87–105.
16. Suárez, F. Estudio de la rotura en barras de acero : aspectos experimentales y numéricos. PhD thesis, Universidad Politécnica de Madrid, 2013.
17. Peters, W.; Ranson, W. Digital imaging techniques in experimental stress analysis. *Optical engineering* **1982**, *21*, 213427–213427.
18. Chu, T.; Ranson, W.; Sutton, M.A. Applications of digital-image-correlation techniques to experimental mechanics. *Experimental mechanics* **1985**, *25*, 232–244.
19. Hung, P.C.; Voloshin, A. In-plane strain measurement by digital image correlation. *Journal of the Brazilian Society of Mechanical Sciences and Engineering* **2003**, *25*, 215–221.
20. Sutton, M.A.; Orteu, J.J.; Schreier, H. *Image correlation for shape, motion and deformation measurements: basic concepts, theory and applications*; Springer Science & Business Media, 2009.
21. Pan, B.; Wang, Z.; Lu, Z. Genuine full-field deformation measurement of an object with complex shape using reliability-guided digital image correlation. *Optics express* **2010**, *18*, 1011–1023.
22. Pan, B.; Dafang, W.; Yong, X. Incremental calculation for large deformation measurement using reliability-guided digital image correlation. *Optics and Lasers in Engineering* **2012**, *50*, 586–592.
23. Suárez, F.; Gálvez, J.C.; Cendón, D.A.; Atienza, J.M. Study of the last part of the stress-deformation curve of construction steels with distinct fracture patterns. *Engineering Fracture Mechanics* **2016**, *166*, 43–59.
24. Guinea, G.; Rojo, F.; Elices, M. Stress intensity factors for internal circular cracks in fibers under tensile loading. *Engineering Fracture Mechanics* **2004**, *71*, 365 – 377.
25. Rojo, F. Aplicación de la mecánica de la fractura a la rotura frágil de fibras de sémola. PhD thesis, Universidad Politécnica de Madrid, 2003.

26. Astm, E. 399-90:" Standard test method for plane-strain fracture toughness of metallic materials. *Annual book of ASTM standards* **1997**, *3*, 506–536.
27. Mirza, M.S.; Barton, D.C.; Church, P.; Sturges, J.L. Ductile Fracture of Pure Copper : An Experimental and Numerical Study. *J. Phys. IV France* **1997**, *07*, 891 – 896.
28. Toribio, J. A fracture criterion for high-strength steel notched bars. *Engineering Fracture Mechanics* **1997**, *57*, 391 – 404.
29. Toribio, J.; Ayaso, F. Anisotropic fracture behaviour of cold drawn steel: a materials science approach. *Materials Science and Engineering: A* **2003**, *343*, 265–272.
30. Toribio, J.; Vergara, D.; Lorenzo, M. Hydrogen effects in multiaxial fracture of cold-drawn pearlitic steel wires. *Engineering Fracture Mechanics* **2017**, *174*, 243–252.
31. Gurson, A.L. *Continuum Theory of Ductile Rupture by Void Nucleation and Growth: Part I. Yield criteria and flow rules for porous ductile media*; Number Part 1 in Technical report (Brown University. Division of Engineering), Division of Engineering, Brown University, 1977.
32. Bridgman, P.W. *Studies in large plastic flow and fracture: with special emphasis on the effects of hydrostatic pressure*; Metallurgy and metallurgical engineering series, Harvard University Press, 1952.
33. Johnson, G.; Cook, W. A constitutive model and data for metals subjected to large strains, high strain rates and high temperatures. *Proceedings of the seventh international symposium on ballistics* **1983**.
34. Bao, Y. Prediction of ductile crack formation in uncracked bodies. PhD thesis, Massachusetts Institute of Technology, 2003.
35. Bao, Y.; Wierzbicki, T. On fracture locus in the equivalent strain and stress triaxiality space. *International Journal of Mechanical Sciences* **2004**, *46*, 81 – 98.
36. Bao, Y. Dependence of ductile crack formation in tensile tests on stress triaxiality, stress and strain ratios. *Engineering Fracture Mechanics* **2005**, *72*, 505 – 522.
37. Borvik, T.; Langseth, M.; Hopperstad, O.; Malo, K. Ballistic penetration of steel plates. *International Journal of Impact Engineering* **1999**, *22*, 855 – 886.
38. Lode, W. Versuche über den Einfluß der mittleren Hauptspannung auf das Fließen der Metalle Eisen, Kupfer und Nickel. *Zeitschrift für Physik A Hadrons and Nuclei* **1926**, *36*, 913–939.
39. Zhang, Z.L.; Thaulow, C.; degård, J.O. A complete Gurson model approach for ductile fracture. *Engineering Fracture Mechanics* **2000**, *67*, 155 – 168.
40. Xue, L.; Wierzbicki, T. Ductile fracture initiation and propagation modeling using a new fracture criterion. 9th European Mechanics of Materials Conference (EMMC9), 2006, pp. 181 – 186.
41. Bai, Y.; Wierzbicki, T. A new model of metal plasticity and fracture with pressure and Lode dependence. *International Journal of Plasticity* **2008**, *24*, 1071 – 1096.
42. Erice, B. Flow and fracture behaviour of high performance alloys. PhD thesis, Universidad Politécnica de Madrid, 2012.
43. Erice, B.; Gálvez, F. A coupled elastoplastic-damage constitutive model with Lode angle dependent failure criterion. *International Journal of Solids and Structures* **2014**, *51*, 93–110.
44. Mirone, G.; Corallo, D. A local viewpoint for evaluating the influence of stress triaxiality and Lode angle on ductile failure and hardening. *International Journal of Plasticity* **2010**, *26*, 348 – 371.
45. Barsoum, I.; Faleskog, J. Micromechanical analysis on the influence of the Lode parameter on void growth and coalescence. *International Journal of Solids and Structures* **2011**, *48*, 925 – 938.
46. Johnson, G.R.; Cook, W.H. Fracture characteristics of three metals subjected to various strains, strain rates, temperatures and pressures. *Engineering Fracture Mechanics* **1985**, *21*, 31 – 48.
47. Sharma, P.; Chandel, P.; Bhardwaj, V.; Singh, M.; Mahajan, P. Ballistic impact response of high strength aluminium alloy 2014-T652 subjected to rigid and deformable projectiles. *Thin-Walled Structures* **2017**.
48. Ouyang, Q.; Weng, G.; Soh, A.; Guo, X. Influences of nanotwin volume fraction on the ballistic performance of coarse-grained metals. *Theoretical and Applied Mechanics Letters* **2017**.
49. Holmen, J.K.; Hopperstad, O.S.; Børvik, T. Influence of yield-surface shape in simulation of ballistic impact. *International Journal of Impact Engineering* **2017**.
50. Sharma, P.; Chandel, P.; Mahajan, P.; Singh, M. Quasi-Brittle Fracture of Aluminium Alloy 2014 under Ballistic Impact. *Procedia Engineering* **2017**, *173*, 206–213.
51. Burley, M.; Campbell, J.; Dean, J.; Clyne, T. Johnson-Cook parameter evaluation from ballistic impact data via iterative FEM modelling. *International Journal of Impact Engineering* **2018**, *112*, 180–192.

564 52. Morales-Alonso, G.; Cendón, D.; Gálvez, F.; Sánchez-Gálvez, V. Influence of the softening curve in the
565 fracture patterns of concrete slabs subjected to blast. *Engineering Fracture Mechanics* **2015**, *140*, 1–16.
566 53. Imbalzano, G.; Tran, P.; Ngo, T.D.; Lee, P.V. A numerical study of auxetic composite panels under blast
567 loadings. *Composite Structures* **2016**, *135*, 339–352.
568 54. Gambirasio, L.; Rizzi, E. An enhanced Johnson–Cook strength model for splitting strain rate and
569 temperature effects on lower yield stress and plastic flow. *Computational Materials Science* **2016**, *113*, 231–265.
570 55. Liang, X.; Wang, Z.; Wang, R. Deformation model and performance optimization research of composite
571 blast resistant wall subjected to blast loading. *Journal of Loss Prevention in the Process Industries* **2017**,
572 *49*, 326–341.
573 56. Wilkins, M.; Streit, R.; Reaugh, J. Cumulative-strain-damage model of ductile fracture: simulation and
574 prediction of engineering fracture tests. Technical report, Lawrence Livermore National Lab., CA (USA);
575 Science Applications, Inc., San Leandro, CA (USA), 1980.
576 57. Lemaitre, J. Coupled elasto-plasticity and damage constitutive equations. *Computer methods in applied*
577 *mechanics and engineering* **1985**, *51*, 31–49.
578 58. Lemaitre, J. A continuous damage mechanics model for ductile fracture. *Transactions of the ASME. Journal*
579 *of Engineering Materials and Technology* **1985**, *107*, 83–89.
580 59. Xue, L. Damage accumulation and fracture initiation in uncracked ductile solids subject to triaxial loading.
581 *International Journal of Solids and Structures* **2007**, *44*, 5163 – 5181.
582 60. Xue, L.; Wierzbicki, T. Ductile fracture initiation and propagation modeling using damage plasticity theory.
583 *Engineering Fracture Mechanics* **2008**, *75*, 3276 – 3293.
584 61. Børvik, T.; Hopperstad, O.; Berstad, T.; Langseth, M. A computational model of viscoplasticity and ductile
585 damage for impact and penetration. *European Journal of Mechanics-A/Solids* **2001**, *20*, 685–712.
586 62. Rice, J.R.; Tracey, D.M. On the ductile enlargement of voids in triaxial stress fields. *Journal of the Mechanics*
587 *and Physics of Solids* **1969**, *17*, 201 – 217.
588 63. Nègre, P.; Steglich, D.; Brocks, W. Crack extension in aluminium welds: a numerical approach using the
589 Gurson–Tvergaard–Needleman model. *Engineering Fracture Mechanics* **2004**, *71*, 2365–2383.
590 64. Fei, H.; Yazzie, K.; Chawla, N.; Jiang, H. The effect of random voids in the modified Gurson model. *Journal*
591 *of electronic materials* **2012**, *41*, 177–183.
592 65. Li, H.; Fu, M.W.; Lu, J.; Yang, H. Ductile fracture: Experiments and computations. *International Journal of*
593 *Plasticity* **2011**, *27*, 147 – 180.
594 66. Needleman, A.; Tvergaard, V. Numerical modeling of the ductile-brittle transition. *International Journal of*
595 *Fracture* **2000**, *101*, 73 – 97.
596 67. Hao, S.; Brocks, W. The Gurson-Tvergaard-Needleman-model for rate and temperature-dependent
597 materials with isotropic and kinematic hardening. *Computational Mechanics* **1997**, *20*, 34–40.
598 68. Steglich, D.; Siegmund, T.; Brocks, W. Micromechanical modeling of damage due to particle cracking in
599 reinforced metals. *Computational Materials Science* **1999**, *16*, 404 – 413.
600 69. Nahshon, K.; Hutchinson, J.W. Modification of the Gurson Model for shear failure. *European Journal of*
601 *Mechanics - A/Solids* **2008**, *27*, 1 – 17.
602 70. Nielsen, K.L.; Tvergaard, V. Effect of a shear modified Gurson model on damage development in a FSW
603 tensile specimen. *International Journal of Solids and Structures* **2009**, *46*, 587 – 601.
604 71. Nahshon, K.; Xue, Z. A modified Gurson model and its application to punch-out experiments. *Engineering*
605 *fracture mechanics* **2009**, *76*, 997–1009.
606 72. Jackiewicz, J. Use of a modified Gurson model approach for the simulation of ductile fracture by growth
607 and coalescence of microvoids under low, medium and high stress triaxiality loadings. *Engineering Fracture*
608 *Mechanics* **2011**, *78*, 487 – 502.
609 73. Nielsen, K.L.; Tvergaard, V. Ductile shear failure or plug failure of spot welds modelled by modified
610 Gurson model. *Engineering Fracture Mechanics* **2010**, *77*, 1031–1047.
611 74. Xu, F.; Zhao, S.; Han, X. Use of a modified Gurson model for the failure behaviour of the clinched joint on
612 Al6061 sheet. *Fatigue & Fracture of Engineering Materials & Structures* **2014**, *37*, 335–348.
613 75. Morgeneyer, T.F.; Besson, J. Flat to slant ductile fracture transition: Tomography examination and
614 simulations using shear-controlled void nucleation. *Scripta Materialia* **2011**, *65*, 1002 – 1005.
615 76. Vadillo, G.; Reboul, J.; Fernández-Sáez, J. A modified Gurson model to account for the influence of the
616 Lode parameter at high triaxialities. *European Journal of Mechanics-A/Solids* **2016**, *56*, 31–44.

77. Hillerborg, A.; Modéer, M.; Petersson, P.E. Analysis of crack formation and crack growth in concrete by means of fracture mechanics and finite elements. *Cement and Concrete Research* **1976**, *6*, 773 – 781.
78. Dugdale, D.S. Yielding of steel sheets containing slits. *Journal of the Mechanics and Physics of Solids* **1960**, *8*, 100 – 104.
79. Vandewalle, L.; Dupont, D. Bending test and interpretation. *RILEM publication PRO* **2003**, *31*, 1–14.
80. RILEM-TCS. Determination of the fracture energy of mortar and concrete by means of three-point bend tests on notched beams. *Materials and Structures* **1985**, *18*, 285–290.
81. Bažant, Z.P.; Planas, J. *Fracture and Size Effect in Concrete and Other Quasibrittle Materials*; New Directions in Civil Engineering, Taylor & Francis, 1997.
82. Bažant, Z.P.; Bittnar, Z.; Jirásek, M.; Mazars, J. *Fracture and Damage in Quasibrittle Structures: Experiment, modeling and computation*; CRC Press, 2004.
83. García-Álvarez, V.O.; Carol, I.; Gettu, R. Numerical simulation of fracture in concrete using joint elements. *Anales de Mecánica de la Fractura* **1994**, pp. 75 – 80.
84. Xie, M.; Gerstle, W. Energy-based cohesive crack propagation modeling. *Journal of Engineering Mechanics* **1995**, *121*, 1349 – 1358.
85. Carol, I.; Prat, P.C.; López, C.M. Normal/Shear Cracking Model: Application to Discrete Crack Analysis. *Journal of Engineering Mechanics* **1997**, *123*, 765 – 773.
86. Cendón, D. Estudio de la fractura en modo mixto de hormigones y morteros. PhD thesis, Universidad Politécnica de Madrid, 2001.
87. Gálvez, J.C.; Cendón, D.A.; Planas, J.; Elices, M. Fractura en modo mixto de probetas de hormigón con doble entalla bajo solicitación de compresión: simulación numérica. *Anales de Mecánica de la Fractura* **2001**, pp. 219 – 225.
88. Gálvez, J.C.; Cervenka, J.; Cendón, D.A.; Saouma, V. A discrete crack approach to normal/shear cracking of concrete. *Cement and Concrete Research* **2002**, *32*, 1567 – 1585.
89. Gálvez, J.C.; Cendón, D.A. Simulación de la fractura del hormigón en modo mixto. *Revista internacional de métodos numéricos* **2002**.
90. Rashid, Y. Ultimate strength analysis of prestressed concrete pressure vessels. *Nuclear engineering and design* **1968**, *7*, 334–344.
91. Suidan, M.; Schnobrich, W.C. Finite element analysis of reinforced concrete. *Journal of the Structural Division* **1973**, *99*.
92. Gupta, A.K.; Akbar, H. Cracking in reinforced concrete analysis. *Journal of Structural Engineering* **1984**, *110*, 1735–1746.
93. De Borst, R.; Nauta, P. Non-orthogonal cracks in a smeared finite element model. *Engineering Computations* **1985**, *2*, 35–46.
94. Jirásek, M.; Zimmermann, T. Rotating crack model with transition to scalar damage. *Journal of engineering mechanics* **1998**, *124*, 277–284.
95. Simo, J.; Oliver, J. A new approach to the analysis and simulation of strain softening in solids. *Fracture and damage in quasibrittle structures* **1994**, pp. 25–39.
96. Larsson, R.; Runesson, K.; Sture, S. Embedded localization band in undrained soil based on regularized strong discontinuity – theory and FE-analysis. *International Journal of Solids and Structures* **1996**, *33*, 3081–3101.
97. Reyes, E. Rotura de la fábrica de ladrillo bajo solicitaciones de tracción y cortante. PhD thesis, Universidad de Castilla la Mancha, 2004.
98. Sancho, J.M.; Planas, J.; Cendón, D.A.; Reyes, E.; Gálvez, J.C. An embedded crack model for finite element analysis of concrete fracture. *Engineering Fracture Mechanics* **2007**, *74*, 75 – 86.
99. Sancho, J.M.; Planas, J.; Fathy, A.M.; Gálvez, J.C.; Cendón, D.A. Three-dimensional simulation of concrete fracture using embedded crack elements without enforcing crack path continuity. *International Journal for Numerical and Analytical Methods in Geomechanics* **2007**, *31*, 173 – 187.
100. Reyes, E.; Gálvez, J.C.; Casati, M.J.; Cendón, D.A.; Sancho, J.M.; Planas, J. An embedded cohesive crack model for finite element analysis of brickwork masonry fracture. *Engineering Fracture Mechanics* **2009**, *76*, 1930 – 1944.

668 101. Gálvez, J.C.; Planas, J.; Sancho, J.M.; Reyes, E.; Cendón, D.A.; Casati, M.J. An embedded cohesive crack
669 model for finite element analysis of quasi-brittle materials. *Engineering Fracture Mechanics* **2012**. Accepted
670 manuscript.
671 102. Siegmund, T.; Brocks, W. A numerical study on the correlation between the work of separation and the
672 dissipation rate in ductile fracture. *Engineering Fracture Mechanics* **2000**, *67*, 139 – 154.
673 103. Scheider, I. Derivation of separation laws for cohesive models in the course of ductile fracture. *Engineering*
674 *Fracture Mechanics* **2009**, *76*, 1450 – 1459.
675 104. ASTM E 1820 - 01. Standard Test Method for Measurement of Fracture Toughness. Technical report, West
676 Conshohocken, PA, 2001.
677 105. Cendón, D.; Jin, N.; Liu, Y.; Berto, F.; Elices, M. Numerical Assessment of Gray Cast Iron Notched
678 Specimens by Using a Triaxiality-Dependent Cohesive Zone Model. *Theoretical and Applied Fracture*
679 *Mechanics* **2017**.